

# The effect of stereochemical constraints on the radius of gyration of folded proteins

Jack A. Logan<sup>a,1</sup>, Jacob Sumner<sup>b,c,2</sup>, Alex T. Grigas<sup>b,c,3</sup>, Mark D. Shattuck<sup>d,4</sup>, and Corey S. O'Hern<sup>a,b,c,e,f,5</sup>

This manuscript was compiled on January 7, 2025

Proteins are composed of linear chains of amino acids that fold into complex three-dimensional structures. A general feature of folded proteins is that they are compact with a radius of gyration  $R_g(N) \sim N^\nu$  that obeys power-law scaling with the number of amino acids  $N$  in each protein and  $\nu \sim 1/3$ . In this study, we investigate the *internal* scaling of the radius of gyration  $R_g(n)$  versus the chemical separation  $n$  between amino acids for all subchains of length  $n$ . We show that for globular proteins  $R_g(n) \sim n^{\nu_{1,2}}$  with a larger exponent  $\nu_1 > 1/3$  for small  $n$  and a smaller exponent  $\nu_2 < 1/3$  for large  $n$ , such that  $R_g(N) \propto N^\nu$ . To describe this scaling behavior for  $R_g(n)$ , we carry out folding simulations for a series of coarse-grained models for proteins beginning with the freely-jointed and freely-rotating chain models composed of spherical monomers and varying degrees of stereochemical constraints. We show that a minimal model, which coarse-grains amino acids into a single spherical backbone atom and one variable-sized spherical side-chain atom, and enforces bend- and dihedral-angle constraints, can recapitulate  $R_g(n)$  for x-ray crystal structures of globular proteins. In addition, this model predicts the correct average packing fraction and size of the hydrophobic core, which are two key physical features that can be used to distinguish between computational ‘decoys’ and correctly folded proteins in protein design applications.

Protein structure | Coarse-grained simulations | Radius of gyration | x-ray crystal structures |

## Introduction

Proteins are polypeptide chains containing tens to thousands of amino acids that carry out important cellular and extracellular functions. While breakthroughs in machine learning have improved our ability to predict the x-ray crystal structures of proteins from their amino acid sequences (1–3) and to design new protein sequences (4), modeling the physical process of protein folding remains a challenge. Experimental studies of protein folding have revealed intermediate kinetic traps, fold switching, mechanisms of misfolding and aggregation, allostery, and structural changes in response to mutations (5–10).

The radius of gyration  $R_g(N)$  of a protein with  $N$  amino acids defined by

$$R_g(N) = \sqrt{\frac{1}{N} \sum_{k=1}^N |\vec{r}_k - \vec{r}_{\text{com}}|^2}, \quad [1]$$

where  $\vec{r}_k$  are the positions of the  $C_\alpha$  atoms and  $\vec{r}_{\text{com}}$  is the center of mass, characterizes its shape and compactness, and has been employed as a reaction coordinate for the folding process (11).  $R_g(N)$  can also be used to identify intrinsically disordered proteins (IDPs), which do not adopt a single compact structure, but contain both open and compact regions. IDPs thus possess larger  $R_g(N)$  compared to compact, globular proteins (12).

The radius of gyration for simple polymers follow power-law scaling relations,  $R_g(N) \propto N^\nu$ , where  $\nu = 1$  for fully extended polymers, 0.5 for random-walk polymers, and 1/3 for collapsed polymers. Recent studies of x-ray crystal structures of globular proteins have shown that  $R_g(N) \sim N^{\nu^*}$  with exponent  $\nu^* \sim 0.33\text{--}0.4$  (13), similar to the behavior for collapsed polymers. (See the inset to Fig. 1 (a).) Deviations from the power-law scaling behavior with exponent  $\nu^*$  are found for proteins with small ratios of hydrophobicity to electric charge (14–19).

## Significance Statement

The structure of proteins strongly influences the functions they perform. The radius of gyration  $R_g$  is often used to characterize the protein folding process and the scaling of  $R_g(n)$  for subchains with chemical separation  $n < N$  for proteins with  $N$  amino acids can be used to classify their structure. In this work, we determine the minimal set of physical features necessary for a coarse-grained model protein to achieve the same scaling  $R_g(n)$  as that found for x-ray crystal structures of globular proteins.

Author affiliations: <sup>a</sup>Department of Mechanical Engineering, Yale University, New Haven, Connecticut 06520, USA; <sup>b</sup>Graduate Program in Computational Biology & Biomedical Informatics, Yale University, New Haven, Connecticut, 06520, USA; <sup>c</sup>Integrated Graduate Program in Physical and Engineering Biology, Yale University, New Haven, Connecticut, 06520, USA; <sup>d</sup>Benjamin Levich Institute and Physics Department, The City College of New York, New York, New York 10031, USA; <sup>e</sup>Department of Applied Physics, Yale University, New Haven, Connecticut, 06520, USA; <sup>f</sup>Department of Physics, Yale University, New Haven, Connecticut, 06520, USA

J.A.L. and J.S. performed the numerical simulations and data analyses. J.A.L., J.S., A.T.G., M.D.S., and C.S.O. wrote and edited the manuscript. J.A.L. and C.S.O. conceptualized the work.

The authors declare no competing interests.

<sup>1</sup> J.A.L. and J.S. contributed equally to this work.

<sup>5</sup>To whom correspondence should be addressed. E-mail: jake.sumner@yale.edu

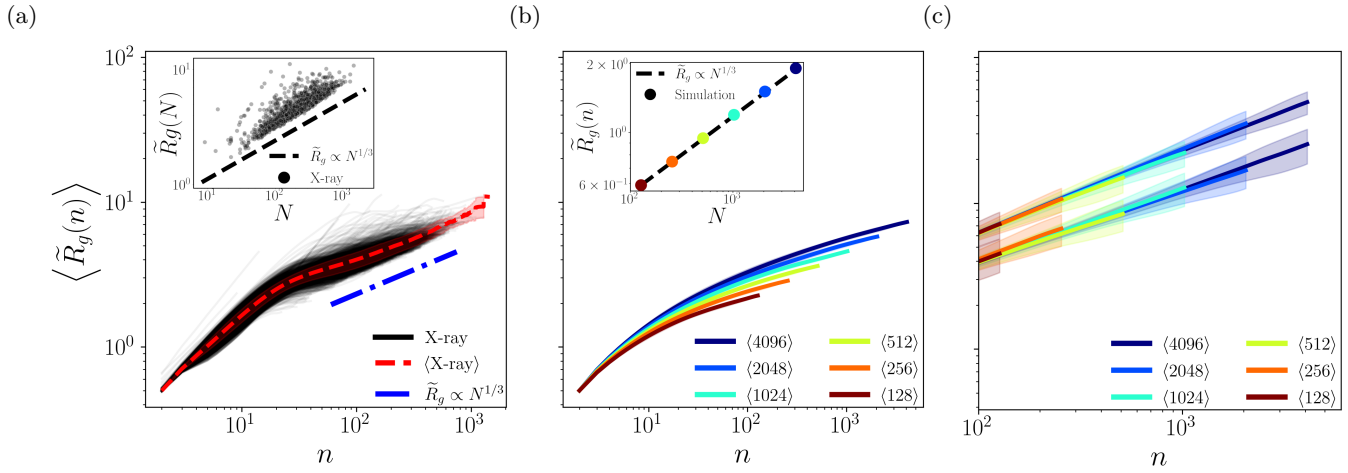


**Fig. 1.** Average normalized radius of gyration  $\langle \tilde{R}_g(n) \rangle$  as a function of the subchain length  $n$ . (a) The anomalous scaling of  $\langle \tilde{R}_g(n) \rangle$  for 2531 x-ray crystal structures of single-chain proteins with variable numbers of amino acids  $N$  (thin black lines). The dashed red line gives the average over all proteins. The dot-dashed blue line has a slope of  $1/3$ . In the inset, we show  $\langle \tilde{R}_g(N) \rangle$  for the same x-ray crystal structures (filled black circles). The dashed black line has a slope of  $1/3$ . (b) For collapsed, excluded-volume bead-spring polymers as for folded proteins,  $\langle \tilde{R}_g(n) \rangle$  does not obey power-law scaling behavior with a *single* exponent. However, in the inset, we show that the endpoints obey  $\tilde{R}_g(N) \propto N^{1/3}$  for  $N = 128$  (black line) to 4096 (violet line) spherical monomers. (c)  $\langle \tilde{R}_g(n) \rangle \propto n^\nu$  with  $\nu \sim 0.59$  for excluded-volume random-walk polymers (upper curves) compared to  $\nu \sim 0.50$  for ideal random-walk polymers (lower curves).

To gain insight into the internal structure of a polymer with  $N$  monomers and positions  $\vec{r}_k$ , we can define  $\langle R_g(n) \rangle$  as the average radius of gyration over all subchains of length  $n$ ,

$$\langle R_g(n) \rangle = \frac{1}{N-n} \sum_{i=1}^{N-n} R_g(i, i+n-1), \quad [2]$$

where

$$R_g(i, j) = \left[ \frac{1}{j-i+1} \sum_{k=i}^j (\vec{r}_k - \langle \vec{r}_k \rangle)^2 \right]^{1/2} \quad [3]$$

and

$$\langle \vec{r}_k \rangle = \frac{1}{j-i+1} \sum_{k=i}^j \vec{r}_k. \quad [4]$$

In Fig. 1 (a), we show that while the endpoint  $R_g$  scaling for folded proteins obeys  $R_g(N) \propto N^{\nu^*}$  with  $\nu^* \sim 0.33-0.4$ , the internal scaling  $R_g(n)$  for folded proteins is more complex.  $R_g(n)$  possesses two characteristic power-law scaling regions:  $R_g(n) \propto n^{\nu_1}$  with  $\nu_1 \sim 0.7 > 1/3$  for small  $n$  and  $\nu_2 \sim 0.2 < 1/3$  for large  $n$ , which differs significantly from  $R_g(n)$  for collapsed bead-spring polymers (Fig. 1 (b)), as well as excluded-volume and ideal random-walk polymers (Fig. 1 (c)). What is the origin of this more complex scaling behavior of the radius of gyration with subchain length  $n$  for folded proteins?

To address this important question, we investigate a range of computational models to determine which best captures the  $R_g(n)$  scaling, as well as other key structural properties that define folded proteins. We focus on four polymer models with increasing complexity: a collapsed excluded-volume bead-spring random-walk polymer model, the previous polymer model with effective bend- and dihedral-angle constraints, the previous polymer model with an additional “side-chain” spherical monomer attached to each backbone monomer, and the previous polymer model except

the sizes of each side-chain spherical monomer are selected to mimic the sidechains of amino acids in the protein. To simplify the polymer models, we do not include explicit attractive interactions between amino acids. Instead, to induce hydrophobic collapse of the polymer models, we employ an external compressive central force with damped molecular dynamics (MD) simulations. Previous studies have shown that the structural properties of bead-spring polymers collapsed using attractive interactions are similar to those for purely repulsive bead-spring polymers compressed using a central force (20). In addition, static packings of purely repulsive, rigid, amino acid-shaped particles compressed to jamming onset (i.e. the maximum packing fraction that does not give rise to overlaps between amino acids) achieve a similar average packing fraction as that found in the cores of x-ray crystal structures of globular proteins (21, 22). This work identifies the minimal coarse-grained model of proteins necessary to recapitulate the scaling of the radius of gyration with chemical distance, as well as other important structural properties of folded proteins, such as the average core packing fraction  $\langle \phi \rangle$ , fraction of amino acids in the core  $f_{\text{core}}$ , and the structure factor  $S(q)$  of the protein backbone. This work provides fundamental insight into the physical features that control the protein folding process and define the structure of folded proteins.

## Methods

In Fig. 2, we show the coarse-grained models of proteins that will be used to determine the physical features of proteins that must be incorporated to recapitulate  $R_g(n)$  and other key structural properties of folded proteins (23–28). All of the polymer models possess a connected backbone including one spherical bead per amino acid backbone with the same average separation between successive  $C_\alpha$  atoms in proteins, i.e.  $\sigma_{bb} \approx 3.8 \text{ \AA}$ . We consider four polymer models with increasing complexity: 1) a collapsed freely-jointed excluded-

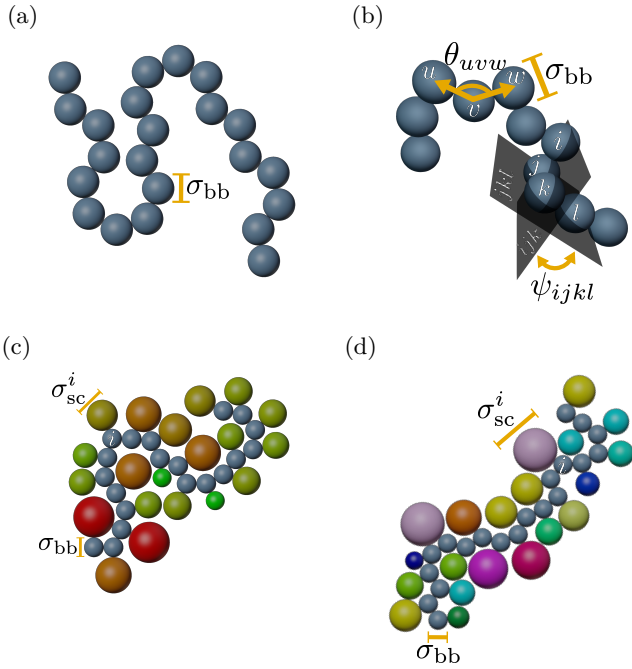


**Fig. 2.** (a)-(d) Snapshots of the four coarse-grained models of proteins, shown as 2D projections. When moving from (a)-(d), the successive models include all features of the previous models.  $\sigma_{\text{bb}}$  indicates the diameter of the spherical bead that represents the backbone of each amino acid. (a) A collapsed freely-jointed excluded-volume random walk (CRW) polymer chain with inter-amino acid separation  $\sigma_{\text{bb}}$ ; (b) For the bend- and dihedral-angle potential (BADA) polymer model, the effective bend angles  $\theta_{uvw}$  between three consecutive amino acids are constrained to values determined by x-ray crystal structures of proteins by a harmonic potential  $U_{\text{bend}}$ , and the effective dihedral angles  $\psi_{ijkl}$  between four consecutive amino acids are constrained to values determined by x-ray crystal structures of proteins by the dihedral angle potential  $U_{\text{dh}}$ . (c) The freely jointed side-chain polymer model (FJSC) includes an additional spherical bead with diameter  $\sigma_{\text{sc}}^i$  (colored by size) chosen randomly from a distribution of amino acid side chain diameters from x-ray crystal structures of proteins that are freely-jointed to each backbone monomer  $i$ ; (d) For the “in-sequence” FJSC (In Seq) polymer model, the diameter of the side chain bead (colored by amino acid) is determined by the amino acid sequence that it is modeling. The example shown is a section of the protein with PDBID: 3ZZO.

volume random-walk (CRW) polymer model, 2) the previous polymer model with constrained effective bend and dihedral angles (BADA) among the backbone spherical beads, 3) the previous polymer model with an additional spherical bead with randomly chosen diameter that is freely-jointed to each backbone monomer to represent the side chain for each amino acid (FJSC), and 4) an “in-sequence” freely-jointed side chain polymer model (In Seq), where the diameter of the side chain bead mimics the size of the side chain of the protein’s amino acid sequence. For each model, we perform more than 2500 independent simulations, one for each protein in a dataset of high-resolution x-ray crystal structures of single-chain proteins. (See Supporting Information (SI) for details of the dataset of proteins.)

In Fig. 2 (a), we illustrate the CRW polymer model, where each of the  $N$  spherical beads represents an amino acid with diameter  $\sigma_{\text{bb}}$ . Neighboring amino acids  $i$  and  $j = i + 1$  are connected using the harmonic bond length potential,

$$U_{\text{bond}}(r_{ij}) = \frac{U_{\text{bb}}}{2} \left( 1 - \frac{r_{ij}}{\sigma_{ij}} \right)^2, \quad [5]$$

where  $r_{ij}$  is the separation between amino acids  $i$  and  $j$ ,  $U_{\text{bb}}$  is the strength of the bond length potential, and  $\sigma_{ij}$  is the sum of the radii of the bonded monomers  $i$  and  $j$ ,  $\sigma_{ij} = (\sigma_i + \sigma_j)/2$ . Non-bonded amino acids interact via the purely repulsive linear spring potential,

$$U_{\text{rep}}(r_{ij}) = \frac{\epsilon_{\text{rep}}}{2} \left( 1 - \frac{r_{ij}}{\sigma_{ij}} \right)^2 \Theta \left( 1 - \frac{r_{ij}}{\sigma_{ij}} \right), \quad [6]$$

where  $\Theta(\cdot)$  is the Heaviside step function and  $\epsilon_{\text{rep}}$  is the strength of the non-bonded repulsive interactions between amino acids. Physical quantities will be made dimensionless using the energy scale  $\epsilon_{\text{rep}}$ , the mass  $m$  of an amino acid backbone, and the lengthscale  $\sigma_{\text{bb}}$ . Throughout this work a tilde over a given symbol is used to denote dimensionless quantities, e.g.  $\tilde{U}_{\text{bb}} = U_{\text{bb}}/\epsilon_{\text{rep}}$ . All dimensionless simulation parameters are defined in the SI.

In Fig. 2 (b), we show that the BADA polymer model also includes constraints on the bend and dihedral angles between amino acids. The bend angles  $\theta_{ijk}$  between three sequential amino acids  $i$ ,  $j = i + 1$ , and  $k = i + 2$  are constrained by

$$U_{\text{bend}}(\theta_{ijk}) = \frac{U_{\text{ba}}}{2} \left( 1 - \frac{\theta_{ijk}}{\theta_{ijk}^0} \right)^2, \quad [7]$$

where the average bend angle  $\theta_{ijk}^0$  is obtained from the x-ray crystal structure dataset. The dihedral-angle potential energy constrains the angle  $\psi_{ijkl}$  between planes formed by the three monomers  $i$ ,  $j$ , and  $k$  and three monomers  $j$ ,  $k$ , and  $l$  among the four consecutive backbone monomers  $i$ ,  $j$ ,  $k$ , and  $l$ :

$$U_{\text{dh}}(\psi_{ijkl}) = U_{\text{da}} \sum_{\langle ijkl \rangle} \sum_{s=1}^4 \left[ A_s \cos(s \psi_{ijkl}) + B_s \sin(s \psi_{ijkl}) \right], \quad [8]$$

where  $U_{\text{da}}$  is the strength of the dihedral-angle potential and the dimensionless coefficients  $A_s$  and  $B_s$  are determined by the x-ray crystal structure dataset. (See SI.)

In Fig. 3 (a), we show the distribution  $\mathcal{P}(\theta_{ijk})$  of bend angles between each set of three successive  $C_{\alpha}$  atoms from the x-ray crystal structure dataset. The distribution has a strong peak around  $\theta_{ijk} \approx 90^\circ$  and a secondary peak near  $120^\circ$ . For each protein that we simulate, we sample the bend angles randomly from  $\mathcal{P}(\theta_{ijk})$ , and then they are constrained using  $U_{\text{bend}}$  in Eq. 7. The dihedral-angle potential energy  $U_{\text{dh}}(\psi_{ijkl})$  (12, 29), as shown in Fig 3 (b), has a global minimum at  $\psi_{ijkl} = \pm 180^\circ$ , a peak near  $60^\circ$ , and a plateau extending over the range  $0^\circ \leq \psi_{ijkl} \leq 120^\circ$ . Calculating the Boltzmann weight for  $U_{\text{dh}}$  will yield  $\mathcal{P}(\psi_{ijkl})$  for the x-ray crystal structure dataset. The key features in  $\mathcal{P}(\theta_{ijk})$  and  $\mathcal{P}(\psi_{ijkl})$  can be attributed to protein secondary structure. The peak around  $\theta_{ijk} \approx 90^\circ$  in  $\mathcal{P}(\theta_{ijk})$  and the plateau in  $\mathcal{P}(\psi_{ijkl})$  originate from  $\alpha$ -helical structures. The secondary peak near  $\theta_{ijk} \approx 120^\circ$  and low-energy tails at  $\psi_{ijkl} = \pm 180^\circ$  stem from  $\beta$ -sheet structures. Note that  $\alpha$ -helices are not favored by the coarse-grained dihedral-angle potential energy  $U_{\text{dh}}$ .

The final two polymer models, FJSC and In Seq in Fig. 2 (c) and (d) incorporate sidechain degrees of freedom, by freely-joining a spherical bead to each backbone bead (using Eq. 5). To approximate the diameter of each sidechain bead, we

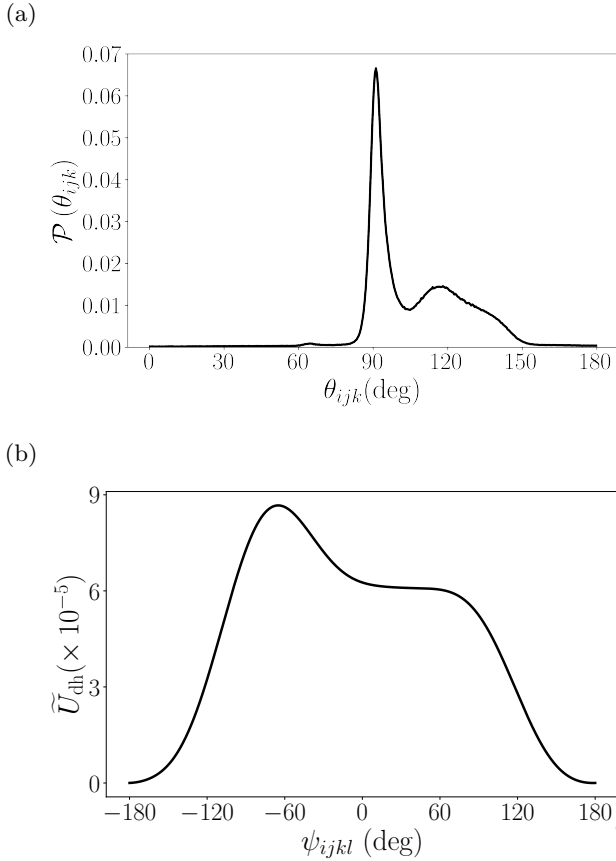


**Fig. 3.** (a) Distribution  $\mathcal{P}(\theta_{ijk})$  of the effective bend angles between three consecutive  $C_\alpha$  atoms from the dataset of x-ray crystal structures of proteins. (b) The dimensionless dihedral-angle potential energy  $\tilde{U}_{\text{dh}}(\psi_{ijkl})$  that yields the distribution  $\mathcal{P}(\psi_{ijkl})$  of effective dihedral angles  $\psi_{ijkl}$  between four consecutive  $C_\alpha$  atoms observed in the x-ray crystal structure dataset when Boltzmann-weighting (12).

calculate the maximum distance between all pairs of atoms in a sidechain and add the average of the radii of the two atoms that are the farthest apart. The selected atomic radii have been used previously to calculate the average packing fraction of amino acids in protein cores (21, 30, 31) and are provided in the SI. Amino acid sidechains can take on many conformations, so each amino acid possesses a distribution of effective side chain diameters. These distributions can either be calculated independently for each amino acid type or binned together to obtain an overall distribution of side chain diameters as shown in Fig. 4. For the FJSC polymer model in Fig. 2 (c), the diameter  $\sigma_{i,\text{sc}}$  of the side chain monomer bonded to backbone monomer  $i$  is chosen randomly from the overall distribution of effective amino acid side chain diameters  $\mathcal{P}(\sigma_{\text{sc}})$  in the main panel of Fig. 4. In contrast, for the In Seq polymer model in Fig. 2 (d), we select the diameter of each sidechain monomer according to the amino sequence of each protein in the x-ray crystal structure dataset. In particular, the diameters of the sidechain monomers are randomly sampled from the individual amino acid sidechain diameter distributions  $\mathcal{P}_i(\sigma_{\text{sc}})$  illustrated in the inset of Fig. 4, where  $\mathcal{P}(\tilde{\sigma}_{\text{sc}}) = A \sum_{i=1}^{20} \mathcal{P}_i(\tilde{\sigma}_{\text{sc}})/A_i$ ,  $A$  is the normalization constant determined by  $\int \mathcal{P}(\tilde{\sigma}_{\text{sc}}) d\tilde{\sigma}_{\text{sc}} = 1$ ,  $A_i = 1/(\Delta\tilde{\sigma}_{\text{sc}} N_c^i)$

is the normalization constant for the diameter distribution of amino acid  $i$  with  $N_c^i$  total counts and bin width  $\Delta\tilde{\sigma}_{\text{sc}}$ .

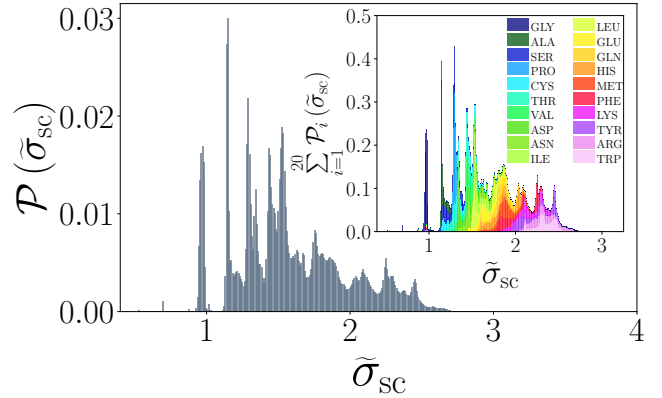


**Fig. 4.** Distribution  $\mathcal{P}(\tilde{\sigma}_{\text{sc}})$  of the effective sidechain diameters (normalized by  $\sigma_{\text{bb}}$ ) binned over all amino acid types. The inset shows the sum of the distributions  $\mathcal{P}_i(\tilde{\sigma}_{\text{sc}})$  for each amino acid type  $i$  indicated by different colors.

When generating initial polymer configurations, the total potential energy contributions,  $U_{\text{rep}}^{\text{tot}} = \sum_{\langle i,j \rangle} U_{\text{rep}}(r_{ij}) \approx 0$  and  $U_{\text{bond}}^{\text{tot}} = \sum_{\langle i,j \rangle} U_{\text{bond}}(r_{ij}) \approx 0$  for all models, and  $U_{\text{bend}}^{\text{tot}} = \sum_{\langle i,j,k \rangle} U_{\text{bend}}(\theta_{ijk}) \approx 0$  for the BADA, FJSC, and In Seq models. We employ damped molecular dynamics (MD) simulations with an additional central force on each bead to generate a collapsed state for each model. We employ a dimensionless damping parameter  $\tilde{\gamma} = 0.1$  in the underdamped limit, and run the damped MD simulations until the maximum magnitude of the net force on any bead  $i$  satisfies  $\max_i \tilde{F}_i < \tilde{F}_{\text{tol}}$ , where  $F_i = |\vec{F}_i| = |\nabla_{\vec{r}_i} U|$ ,  $U$  is the total potential energy for a given polymer model, and  $\tilde{F}_{\text{tol}} = 5 \times 10^{-13}$ . We include an extra factor of the ratio of the bead diameter  $\sigma_i$  to the maximum bead diameter  $\sigma_{\text{max}}$  raised to a power in the expression for the central force to ensure that the polymer does form clusters of similar-sized beads during collapse when the beads are polydisperse (20):

$$\vec{F}_{\text{cent}} = -F_{\text{cent}} \left( \frac{\sigma_i}{\sigma_{\text{max}}} \right)^{9/4} \hat{\mathbf{r}}_i. \quad [9]$$

The strength of the central force  $\tilde{F}_{\text{cent}} = 10^{-4}$  compared to the constraint forces is such that the constraints remain satisfied during polymer collapse, e.g., the bend and dihedral angle distributions  $\mathcal{P}(\theta_{ijk})$  and  $\mathcal{P}(\psi_{ijkl})$  are nearly identical in the collapsed and initial states, and the results do not depend on  $\tilde{F}_{\text{cent}}$ . We calculate the dimensionless radius of gyration  $\tilde{R}_g(n)$  for the positions of the backbone beads and other structural properties in each collapsed state for each polymer model and for each x-ray crystal structure.

## Results & Discussion

The results for the normalized radius of gyration  $\langle \tilde{R}_g(n) \rangle$  as a function of subchain length  $n$  for the four polymer models and the dataset of x-ray crystal structures are shown in Fig. 5 (a). (We also show examples of the collapsed structures for each of the four polymer models in the SI.) To quantify differences in the radius of gyration between each polymer model and the x-ray crystal structure dataset, we compute the normalized

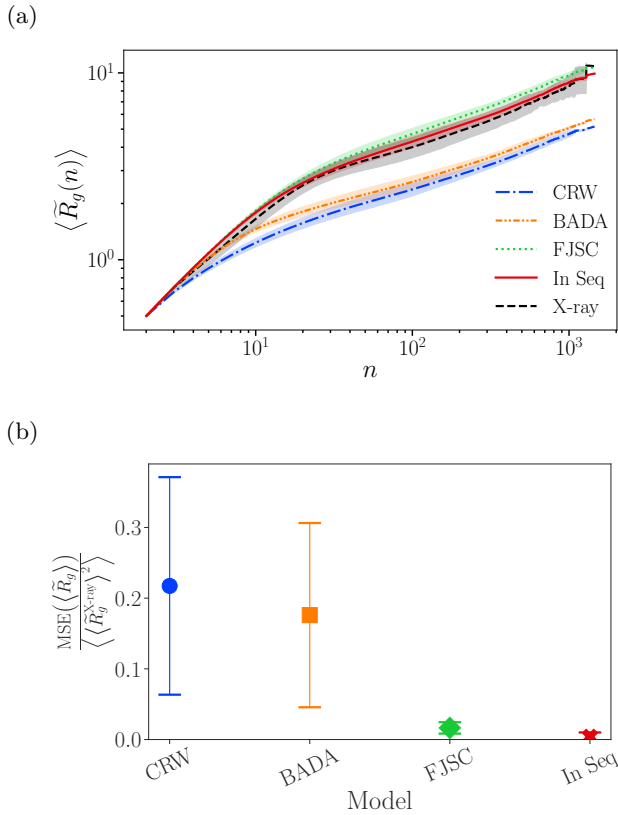


**Fig. 5.** (a) The average radius of gyration  $\langle \tilde{R}_g \rangle$  plotted versus subchain length  $n$  for the x-ray crystal structures (black dashed line) and polymer models with corresponding colors and line styles in the legend. The shading indicates the standard deviation about  $\langle \tilde{R}_g \rangle$  for each dataset. (b) Normalized mean-squared error in Eq. 10 between  $\langle \tilde{R}_g(n) \rangle$  for each polymer model and the average over the x-ray crystal structures.

mean-squared error (MSE) in  $R_g(n)$ :

$$\text{MSE}(\langle \tilde{R}_g \rangle) = \frac{\sum_{n=2}^N \left( \Delta \langle \tilde{R}_g(n) \rangle \right)^2}{\sum_{n=2}^N \left( \langle \tilde{R}_g^{\text{x-ray}}(n) \rangle \right)^2}, \quad [10]$$

where  $\Delta \langle \tilde{R}_g(n) \rangle = \langle \tilde{R}_g^{\text{model}}(n) \rangle - \langle \tilde{R}_g^{\text{x-ray}}(n) \rangle$ .

As shown in Fig. 5 (a), the simplest polymer model (CRW) does not recapitulate  $\langle R_g(n) \rangle$  for folded proteins.  $\langle R_g(n) \rangle$  for the CRW model is highly curved on a log-log plot (i.e. does not possess a kink) at small  $n$  and is a factor of  $\sim 1.5$  smaller than  $\langle R_g(n) \rangle$  for the x-ray crystal structure data at large  $n$ . The CRW polymer model has the largest normalized mean-squared error relative to the x-ray crystal structure data of the four models we considered, as shown in Fig 5 (b).

Introducing effective bend- and dihedral-angle potentials leads to a small, but important change in  $\langle R_g(n) \rangle$  for the BADA polymer model, i.e., the appearance of a kink near  $n^* \sim 10$  that separates the small- and large- $n$  regions.  $\langle R_g(n) \rangle \sim n^{\nu_1, 2}$ , where  $\nu_1 \sim 0.2$  for  $n \lesssim n^*$  and  $\nu_2 \sim 0.7$  for  $n \gtrsim n^*$ , which is similar to the results for the x-ray crystal structure data. However,  $n^*$  for the BADA polymer model is smaller than that for the x-ray crystal structure data, and the normalized MSE for the BADA model is still quite

large ( $\sim 0.2$ ). The large MSE is caused by the fact that the persistence length of subchains in the BADA model is shorter than that for the x-ray crystal structures, and the effective bend- and dihedral-angle constraints are not sufficient to keep the subchains from over-collapsing at small  $n$ .

When the amino acids are coarse-grained to include both backbone and sidechain monomers (i.e. the FJSC and In Seq polymer models), the backbone can no longer collapse as densely as found for the CRW and BADA models. For the FJSC and In Seq models, the kink location increases to  $n^* \sim 30$  and their  $\langle R_g(n) \rangle$  are similar to that for the x-ray crystal structure data. The normalized MSE is  $\lesssim 0.02$  for both the FJSC and In Seq polymer models.

To determine how well the FJSC and In Seq polymer models can describe the structural properties of folded proteins, we also calculate the average core packing fraction  $\langle \phi \rangle$ , average fraction of amino acids that occur in the core  $\langle f_{\text{core}} \rangle$ , and the average structure factor  $\langle S(q) \rangle$  for the polymer models and x-ray crystal structures.  $\langle \phi \rangle$  and  $\langle f_{\text{core}} \rangle$  are among the most important physical features of protein cores and can be used to distinguish x-ray crystal structures of proteins from computationally-generated protein “decoys” (32, 33). In addition,  $S(q)$  can be used to quantify protein structure outside of the core. Thus, a coarse-grained polymer model is a high-quality representation of folded proteins if it recapitulates these quantities in addition to  $\langle R_g(n) \rangle$ .

Protein cores are dense packings of amino acids in the interior of proteins, whose size and structure have been directly correlated with the stability of the protein (34, 35). Previous studies have shown that the average core packing fraction in x-ray crystal structures of proteins is  $\langle \phi \rangle \approx 0.55$  (21, 30, 33). To identify core amino acids, we implement the software FreeSASA (36) to compute the relative solvent accessible surface area (rSASA) using the Lee-Richards algorithm (37). This method employs a probe sphere to represent a solvent molecule of diameter  $\tilde{\sigma}_{\text{probe}}$  that rolls over the folded protein to determine how much surface area of each amino acid it can make contact with relative to the total surface area of the fully solvated amino acid. In this work, we consider an amino acid to be in the core if  $\text{rSASA} \leq 10^{-3}$ , which has been previously used as an effective rSASA cutoff for identifying core amino acids (20, 30–33, 38). Smaller diameter probes can access amino acids that are buried deeper in the protein because they can fit through smaller void spaces. Thus, we expect that as the probe shrinks, the number of amino acids found in the core will decrease and when  $\tilde{\sigma}_{\text{probe}} \rightarrow 0$  the entire protein will be labeled as “surface”, with  $f_{\text{core}} = 0$ . Because proteins typically reside in water, we used a probe sphere with a diameter given by the size of a water molecule,  $\sigma_{\text{H}_2\text{O}} \approx 0.73\sigma_{\text{bb}}$ . Core amino acids in x-ray crystal structures are often not all nearest neighbors and instead occur in separate clusters. Motivated by this, we measure the average *local* packing fraction  $\langle \phi \rangle$  for each polymer configuration or x-ray crystal structure. To calculate  $\langle \phi \rangle$ , we perform a Voronoi tessellation and find the ratio of the volume  $V_i$  of amino acid  $i$  to the local Voronoi cell volume  $V_i^{\text{voro}}$  of amino acid  $i$ , averaged over all  $N_{\text{core}}$  core amino acids:

$$\langle \phi \rangle = \frac{1}{N_{\text{core}}} \sum_{i=1}^{N_{\text{core}}} \frac{V_i}{V_i^{\text{voro}}}. \quad [11]$$

The fraction of core amino acids is given by  $f_{\text{core}} = N_{\text{core}}/N$ .  $\langle\phi\rangle$  and  $f_{\text{core}}$  for the x-ray crystal structures are found using Voronoi tessellation, as described above, but with atomic radii used in previous studies (21, 30, 31). The SI includes additional details concerning calculations of the local packing fraction, fraction of core amino acids, and rSASA.

$\langle\phi\rangle$  and  $\langle f_{\text{core}}\rangle$  for the polymer models are compared to the corresponding values for the x-ray crystal structures in Fig. 6 (a) and (b). We find that the CRW polymer model yields the densest core packing compared to all other polymer models with  $\langle\phi\rangle \approx 0.66$ , which is much larger than  $\langle\phi\rangle = 0.55$  for the cores of x-ray crystal structures of proteins. The CRW polymers are composed of spherical beads that all have the same size and possess elevated values of the local bond-orientational order parameter, which explains why the local packing fraction of the core of CRW polymers is  $\langle\phi\rangle > \phi_{\text{rcp}} \approx 0.64$  for static packings of monodisperse spheres (39, 40), as well as collapsed freely-jointed chains (41–47). Consistent with this result, we also find that a much larger fraction of the amino acids occur in the core ( $f_{\text{core}} \sim 0.37$ ) compared to the results for x-ray crystal structures of proteins.

For the BADA polymer model, which includes constraints on the effective bend and dihedral angles, the local packing fraction decreases significantly ( $\langle\phi\rangle \approx 0.56$ ) compared to the CRW polymer model. The effective bend- and dihedral-angle constraints decrease the packing fraction by restricting dense monomer packing for subchains with small  $n$ , and thus increasing the void space in BADA polymers. The lower core packing fraction leads to increased separation between  $C_{\alpha}$  atoms, which reduces the size of the core to  $\langle f_{\text{core}}\rangle \sim 0.2$ . However, this value is still much larger than  $\langle f_{\text{core}}\rangle \sim 0.08$  for x-ray crystal structures of proteins.

Adding sidechain beads in the FJSC polymer model appears to have a surprising effect on the local packing fraction in the core.  $\langle\phi\rangle \approx 0.58$  for FJSC, which is slightly larger than that for the BADA polymer model. There are several possible reasons for this result. First, the FJSC representation of amino acids does not include intra-residue bonded atomic overlaps, in contrast to the all-atom models of x-ray crystal structures. Second, the size of the single-bead sidechain representation in the FJSC model are chosen randomly, not according to the amino acid sequence, which gives rise to additional void space not found in x-ray crystal structures of proteins. The amino acid sequences of proteins have evolved to fold into compact structures, while random sequences of amino acids lead to frustration that causes the cores to be much smaller than those in x-ray crystal structures. These hypotheses are supported by the results for the In Seq polymer model, where  $\langle\phi\rangle \approx 0.567$  and  $\langle f_{\text{core}}\rangle \sim 0.05$ , which are both within error of the values for x-ray crystal structures.

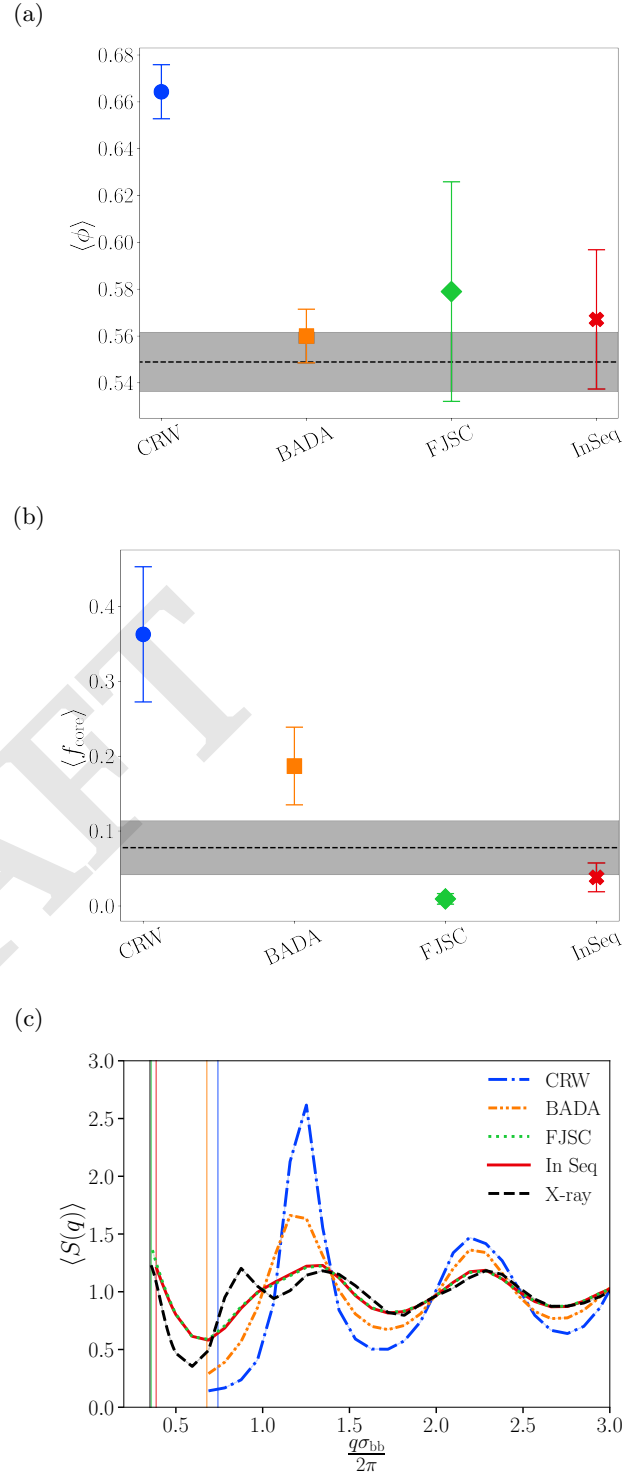


**Fig. 6.** For each polymer model indicated by the colors and line types in the legend, we compare (a) the average local packing fraction  $\langle\phi\rangle$ , (b) the average fraction of amino acids in the core  $\langle f_{\text{core}}\rangle$ , and (c) the average structure factor  $\langle S(q)\rangle$ . The vertical lines in (c) indicate the wavenumbers  $q = 2\pi/\max\{\langle\tilde{R}_g(N)\rangle\}$  for each polymer model. In panels (a) and (b), the horizontal dashed black line marks the average values for the x-ray crystal structures with  $\pm 1$  standard deviation shaded in gray. The error bars for the data points in (a) and (b) represent the standard deviation of the distributions for each polymer model.

In Fig. 6 (c), we compare the average structure factor  $\langle S(q)\rangle$  obtained from the  $C_{\alpha}$  atom positions for each polymer

model and the x-ray crystal structures. The most obvious difference between  $\langle S(q) \rangle$  among the polymer models is the amplitude of the first and second peaks. The CRW and BADA polymer models have the largest amplitudes, which implies short-range ordering that is not found in the x-ray crystal structures.  $\langle S(q) \rangle$  for the polymer models with single sidechain beads are very similar to each other and nearly identical to  $\langle S(q) \rangle$  for the x-ray crystal structures for  $q\sigma_{\text{bb}}/(2\pi) > 1.0$ . For wavenumbers  $\sigma_{\text{bb}}/\max\{\langle \tilde{R}_g(N) \rangle\} < q\sigma_{\text{bb}}/(2\pi) < 1$ ,  $\langle S(q) \rangle$  for the x-ray crystal structures possesses a small peak that is not captured by the FJSC and In Seq polymer models. This low- $q$  peak implies long wavelength spatial correlations in the x-ray crystal structures that are not present in the polymer models.

## Conclusions and Outlook

Using a series of coarse-grained polymer models with increasing complexity, we identified the important physical features that are required to accurately describe the structural properties of folded proteins, obtained from a dataset of more than 2500 high-resolution x-ray crystal structures of single-chain proteins. In particular, sidechain degrees of freedom are necessary to recapitulate the novel  $\langle R_g(n) \rangle$  scaling with subchain length  $n$  for x-ray crystal structures of proteins shown in Fig. 1. Both the FJSC and In Seq polymer models yield  $\lesssim 0.02$  in the normalized mean-squared error compared to  $\langle R_g(n) \rangle$  for the x-ray crystal structures. However, the FJSC polymer model, which randomly assigns the sizes of the sidechain beads (among typical sizes of amino acid side chains), does not accurately describe the average local packing fraction  $\langle \phi \rangle$  of core amino acids and fraction  $\langle f_{\text{core}} \rangle$  of core amino acids of x-ray crystal structures of proteins. In contrast, the In Seq polymer model, where the size of each sidechain bead matches that of each amino acid in the given protein, recapitulates  $\langle \phi \rangle \sim 0.55$  and  $\langle f_{\text{core}} \rangle \sim 0.08$  in x-ray crystal structures of proteins. This result emphasizes the important coupling between the local packing of core amino acids and amino acid sequence in proteins.

The results for  $\langle S(q) \rangle$  raise interesting questions for future work.  $\langle S(q) \rangle$  for the In Seq polymer model matches that for the x-ray crystal structures for  $q\sigma_{\text{bb}}/(2\pi) > 1.0$ . However,  $\langle S(q) \rangle$  for the x-ray crystal structures possesses long-wavelength correlations that are not captured by the In Seq polymer model. The current polymer models describe the structural properties of the cores of folded proteins *on average*, i.e. the root-mean-square deviations (RMSD) in the  $C_\alpha$  positions between the In Seq polymer model for a given protein and the x-ray crystal structure of that protein are greater than 5 Å.

These results show that the In Seq polymer model can accurately capture the average structural properties of folded proteins, while being highly coarse-grained. In addition, the results emphasize the importance of the distributions of the effective bend and dihedral angles of the amino acid backbone, as well as the sequence-dependent sizes of the sidechains. We note that the anisotropic geometry of amino acids is less important in determining the average behavior of  $\langle R_g(n) \rangle$ ,  $f_{\text{core}}$ , and  $\langle \phi \rangle$  for protein cores.

The polymer models can be improved in several ways to model the structural properties of individual proteins, rather than the average properties. First, the resolution

of the polymer models can be increased by using multiple beads to represent the backbone and sidechain of each amino acid as described in our recent studies of the collapse of all-atom models of proteins with purely repulsive interactions, or using other coarse-grained models (48) or all-atom force fields. Using a compressive spring force with damped molecular dynamics simulations in this work to collapse the polymer models has advantages and disadvantages. An advantage is that it enables rapid collapse of the polymer models. However, the spring force we implement is isotropic, and thus the collapsed polymers do not possess anisotropy at large length scales as found in some proteins. In future studies, we can add attractive interactions based on the hydrophobicity and polarity of amino acids, which have been calibrated in previous studies to yield native-like folds. We can start with a partially unfolded In Seq polymer, and cool the polymer slowly to obtain the collapsed structure. By varying the cooling rate, we will be able to achieve collapsed In Seq models with minimal  $C_\alpha$  RMSD from the reference protein x-ray crystal structure.

1. J Abramson, et al., Accurate structure prediction of biomolecular interactions with AlphaFold 3. *Nature* **630**, 493–500 (2024).
2. M Baek, et al., Accurate prediction of protein structures and interactions using a three-track neural network. *Science* **373**, 871–876 (2021).
3. Z Lin, et al., Evolutionary-scale prediction of atomic-level protein structure with a language model. *Science* **379**, 1123–1130 (2023).
4. J Dauparas, et al., Robust deep learning–based protein sequence design using ProteinMPNN. *Science* **378**, 49–56 (2022).
5. CB Anfinsen, Principles that govern the folding of protein chains. *Science* **181**, 223–230 (1973).
6. LL Porter, LL Looger, Extant fold-switching proteins are widespread. *Proc. Natl. Acad. Sci.* **115**, 5968–5973 (2018) Publisher: Proceedings of the National Academy of Sciences.
7. CM Dobson, Protein misfolding, evolution and disease. *Trends Biochem. Sci.* **24**, 329–332 (1999).
8. J Monod, J Wyman, JP Changeux, On the nature of allosteric transitions: A plausible model. *J. Mol. Biol.* **12**, 88–118 (1965).
9. AR Fersht, A Matouschek, L Serrano, The folding of an enzyme: I. Theory of protein engineering analysis of stability and pathway of protein folding. *J. Mol. Biol.* **224**, 771–782 (1992).
10. M Grubele, K Dave, S Sukenik, Globular protein folding in vitro and in vivo. *Annu. Rev. Biophys.* **45**, 233–251 (2016).
11. E Yamamoto, T Akimoto, A Mitsutake, R Metzler, Universal relation between instantaneous diffusivity and radius of gyration of proteins in aqueous solution. *Phys. Rev. Lett.* **126**, 128101 (2021).
12. WW Smith, PY Ho, CS O'Hern, Calibrated Langevin-dynamics simulations of intrinsically disordered proteins. *Phys. Rev. E* **90**, 042709 (2014).
13. L Hong, J Lei, Scaling law for the radius of gyration of proteins and its dependence on hydrophobicity. *J. Polym. Sci. Part B: Polym. Phys.* **47**, 207–214 (2009).
14. G Damaschun, et al., Streptokinase is a flexible multi-domain protein. *Eur. Biophys. J.* **20**, 355–361 (1992).
15. EE Lattman, Small angle scattering studies of protein folding. *Curr. Opin. Struct. Biol.* **4**, 87–92 (1994).
16. M Kataoka, Y Goto, X-ray solution scattering studies of protein folding. *Fold. Des.* **1**, R107–R114 (1996).
17. H Durchschlag, P Zipper, G Purr, R Jaenicke, Comparative studies of structural properties and conformational changes of proteins by analytical ultracentrifugation and other techniques. *Colloid Polym. Sci.* **274**, 117–137 (1996).
18. Y Mei, et al., Structural changes and chain radius of gyration in cold-drawn polyethylene after annealing: small- and wide-angle x-ray scattering and small-angle neutron scattering studies. *The J. Phys. Chem. B* **109**, 16650–16657 (2005).
19. R Biehl, M Monkenbusch, D Richter, Exploring internal protein dynamics by neutron spin echo spectroscopy. *Soft Matter* **7**, 1299–1307 (2011).
20. AT Grigas, A Fisher, MD Shattuck, CS O'Hern, Connecting polymer collapse and the onset of jamming. *Phys. Rev. E* **109**, 034406 (2024).
21. JC Gaines, WW Smith, L Regan, CS O'Hern, Random close packing in protein cores. *Phys. Rev. E* **93**, 032415 (2016).
22. Z Mei, et al., Analyses of protein cores reveal fundamental differences between solution and crystal structures. *Proteins: Struct. Funct. Bioinforma.* **88**, 1154–1161 (2020).
23. H Taketomi, Y Ueda, N Gö, Studies on Protein Folding, Unfolding and Fluctuations by Computer Simulation. *Int. J. Pept. Protein Res.* **7**, 445–459 (1975).
24. I Bahar, AR Atlgan, B Erman, Direct evaluation of thermal fluctuations in proteins using a single-parameter harmonic potential. *Fold. & Des.* **2**, 173–181 (1997).
25. P Derreumaux, From polypeptide sequences to structures using Monte Carlo simulations and an optimized potential. *The J. Chem. Phys.* **111**, 2301–2310 (1999).
26. A Kolinski, Protein modeling and structure prediction with a reduced representation. *Acta Biochimica Polonica* **51**, 349–371 (2004).

27. P Kar, SM Gopal, YM Cheng, A Predeus, M Feig, PRIMO: A transferable coarse-grained force field for proteins. *J. Chem. Theory Comput.* **9**, 3769–3788 (2013).
28. A Davtyan, et al., AWSEM-MD: protein structure prediction using coarse-grained physical potentials and bioinformatically based local structure biasing. *The J. Phys. Chem. B* **116**, 8494–8503 (2012).
29. C Chen, et al., A comparison of united atom, explicit atom, and coarse-grained simulation models for poly (ethylene oxide). *The J. Chem. Phys.* **124** (2006).
30. JC Gaines, AH Clark, L Regan, CS O'Hern, Packing in protein cores. *J. Physics: Condens. Matter* **29**, 293001 (2017).
31. JD Treado, Z Mei, L Regan, CS O'Hern, Void distributions reveal structural link between jammed packings and protein cores. *Phys. Rev. E* **99**, 022416 (2019).
32. AT Grigas, et al., Using physical features of protein core packing to distinguish real proteins from decoys. *Protein Sci.* **29**, 1931–1944 (2020).
33. AT Grigas, Z Liu, L Regan, CS O'Hern, Core packing of well-defined x-ray and nmr structures is the same. *Protein Sci.* **31**, e4373 (2022).
34. KA Dill, Dominant forces in protein folding. *Biochemistry* **29**, 7133–7155 (1990).
35. J Liang, KA Dill, Are proteins well-packed? *Biophys. J.* **81**, 751–766 (2001).
36. S Mitternacht, Freesasa: An open source c library for solvent accessible surface area calculations. *F1000Research* **5** (2016).
37. B Lee, FM Richards, The interpretation of protein structures: estimation of static accessibility. *J. Mol. Biol.* **55**, 379–IN4 (1971).
38. J Gaines, et al., Comparing side chain packing in soluble proteins, protein-protein interfaces, and transmembrane proteins. *Proteins: Struct. Funct. Bioinforma.* **86**, 581–591 (2018).
39. CS O'Hern, SA Langer, AJ Liu, SR Nagel, Random packings of frictionless particles. *Phys. Rev. Lett.* **88**, 075507 (2002).
40. K Zhang, et al., Connection between the packing efficiency of binary hard spheres and the glass-forming ability of bulk metallic glasses. *Phys. Rev. E* **90**, 032311 (2014).
41. M Laso, NC Karayiannis, K Foteinopoulou, ML Mansfield, M Kröger, Random packing of model polymers: local structure, topological hindrance and universal scaling. *Soft Matter* **5**, 1762–1770 (2009).
42. NC Karayiannis, K Foteinopoulou, M Laso, Contact network in nearly jammed disordered packings of hard-sphere chains. *Phys. Rev. E* **80**, 011307 (2009).
43. NC Karayiannis, K Foteinopoulou, M Laso, The structure of random packings of freely jointed chains of tangent hard spheres. *The J. Chem. Phys.* **130** (2009).
44. RS Hoy, CS O'Hern, Minimal Energy Packings and Collapse of Sticky Tangent Hard-Sphere Polymers. *Phys. Rev. Lett.* **105**, 068001 (2010) Publisher: American Physical Society.
45. RS Hoy, NC Karayiannis, Simple crystallizable bead-spring polymer model (2013) arXiv:1303.5494 [cond-mat].
46. RS Hoy, J Harwayne-Gidansky, CS O'Hern, Minimal energy packings of nearly flexible polymers. *The J. Chem. Phys.* **138**, 054905 (2013).
47. KA Interiano-Alberto, PK Morse, RS Hoy, Critical-like slowdown in thermal soft-sphere glasses via energy minimization. *Phys. Rev. E* **109**, L062603 (2024).
48. PC Souza, et al., Martini 3: A general purpose force field for coarse-grained molecular dynamics. *Nat. Methods* **18**, 382–388 (2021).